applied sciences

MDPI

Article

Quasi-Static Finite Cylindrical Cavity Expansion Model for Long-Rod Penetration into Cylindrical Metal Thick Targets with Finite Diameters

Yunke Lu, Xigui Tao *, Yicun Chen, Bei Zhang *, Jiageng Song, Xiangyu Xu and Jianshuai Wang

Institute of Defense Engineering, Academy of Military Sciences (AMS), PLA, Beijing 100850, China; nudtluyunke@outlook.com (Y.L.); cyc-lgdx@foxmail.com (Y.C.); 18855170117@163.com (J.S.); 2019201001@tju.edu.cn (X.X.); 15200035795@163.com (J.W.)

* Correspondence: tonytxg@126.com (X.T.); zhangbei_qd@163.com (B.Z.)

Abstract: A quasi-static finite cavity cylindrical expansion model is proposed to investigate the lateral boundary effect during long-rod penetration. Analytical solutions for the cavity pressure in the elastic–plastic stage and plastic stage are obtained, through which a decay function for the lateral boundary effect is constructed. The resistance of the target with finite diameter R_T is obtained by multiplying the decay function with the resistance of infinite target R_T*. Then, a theoretical model for the penetration into the metal targets with finite diameters by long rods is proposed by substituting R_T into the Alekseevskii–Tate model. The proposed model is verified by comparison with existing experimental results. Furthermore, the effect of the target diameter, initial impact velocity and yield criterion on the penetration depth and resistance are investigated. The results showed that the lateral boundary effect should be taken into account if the ratio of the target radius to the rod radius (r_{t0}/R_P) is less than 25.

Keywords: impact dynamics; long-rod penetration; quasi-static finite cylindrical cavity expansion model; lateral boundary effect; target resistance; metal target

check for updates

Citation: Lu, Y.; Tao, X.; Chen, Y.; Zhang, B.; Song, J.; Xu, X.; Wang, J. Quasi-Static Finite Cylindrical Cavity Expansion Model for Long-Rod Penetration into Cylindrical Metal Thick Targets with Finite Diameters. *Appl. Sci.* **2024**, *14*, 1523. https://doi.org/10.3390/app14041523

Academic Editor: Kang Su Kim

Received: 12 January 2024
Revised: 31 January 2024
Accepted: 6 February 2024
Published: 14 February 2024

Copyright: © 2024 by the authors. Licensee MDPI, Basel, Switzerland. This article is an open access article distributed under the terms and conditions of the Creative Commons Attribution (CC BY) license (https://creativecommons.org/licenses/by/4.0/).

1. Introduction

The problem of long-rod penetration has been extensively researched in the disciplines of protective engineering and armor and weapon design recently [1–3]. Unlike rigid projectile penetration, long-rod penetration will cause severe erosion at the contact area between the long-rod and the target, with a semi-fluid deformation mode. In the 1960s, Alekseevskii [4] and Tate [5,6] proposed a theoretical model for the high-speed penetration of long-rods (the Alekseevskii–Tate model). This model assumes that the projectile tail remains rigid during penetration and that erosion occurs only near the contact surface between the projectile and the target. By introducing the projectile strength term Y_P and the target resistance term R_T, the Alekseevskii–Tate model modifies the Bernoulli equation to take into account the strength properties. Subsequent studies have expanded the Alekseevskii–Tate model by considering the effective cross-sectional area [7], transient response stage [8], projectile head shape [9], target response region [10], and target material viscosity [11]. Calculating the appropriate R_T is the main focus and challenge in the aforementioned models. Previous studies [6] have demonstrated that utilizing a cavity expansion model to derive R_T can yield accurate results.

Bishop [12] first proposed the cavity expansion model, which was primarily used to investigate the issue of normal penetration into semi-infinite targets. Forrestal et al. [13,14] conducted studies on the penetration of rigid projectiles into semi-infinite metal and concrete targets using the cavity expansion model. On this basis, Chen and Li [15] investigated the shape of warheads and proposed a dimensionless head shape function. However, the penetration of finite-diameter targets violates the semi-infinite assumption in the traditional

cavity expansion model, thus requiring the introduction of a finite cavity expansion model. Macek et al. [16] first proposed the finite spherical cavity expansion model to study the penetration problem of layered geological materials, taking into account boundary and layering effects.

Recent years have seen the finite cavity expansion model extended to metal [17] and concrete [18] targets, and applied to the study of penetration trajectories [19], perforation [20], and penetration of finite-diameter targets [21,22]. However, the extended model still only applies to rigid projectiles and not to eroding rods directly. Experimental results [23,24] suggest that a long-rod projectile penetrating targets of different diameters at high speed may experience a deviation of approximately 30% in penetration depth. To analyze the influence of the target diameter on high-speed long-rod penetration, Jiang [25] proposed the dynamic finite cylindrical cavity expansion model. It was found that the dynamic resistance is free from the target diameter. He then derived R_T based on the average quasi-static cavity pressure instead of the semi-empirical formula in the Alekseevskii–Tate model, thus obtaining the earliest theoretical model of high-speed long-rod penetration into finite-diameter metal targets. However, it is necessary to derive the strength of the target material from the R_T obtained from numerical simulations. Furthermore, the use of the dynamic cavity expansion model to calculate quasi-static resistance does not consider the influence of the lateral boundary expansion of the targets. Wang [26] subsequently introduced the unified strength model to analyze different yield criteria. The results showed that different yield criteria can cause a maximum depth change of 15.93%. However, the selection of the yield criterion is dependent on the results of the penetration data.

In summary, while there has been extensive research on the penetration of rigid projectiles, the research on the penetration of long rods into finite-diameter metal targets is insufficient. Considering the displacement of the target, a quasi-static finite cylindrical cavity expansion model for elastic–plastic materials with unified strength theory is proposed and a decay function for the lateral boundary effect is constructed. Then, by combining the decay function and the Alekseevskii–Tate model, an analytical model for the high-speed penetration of finite-diameter metal targets by long rods is established. The model in this paper is verified by experimental and numerical results. Finally, the effects of target diameter, initial impact velocity, and yield criterion on penetration depth and target resistance are examined in detail.

2. Quasi-Static Finite Cylindrical Cavity Expansion Model

In this section, an analytical model for the responses of a finite metal target from the uniform expansion of a cylindrically symmetric cavity is developed. The responses are divided into elastic–plastic and plastic stages based on the size of the cavity radius. Analytical solutions for the cavity pressure are then obtained separately. Based on the solution, the decay function for the lateral boundary effect is obtained using the principle of energy equivalence.

2.1. Basic Model and Equations

It is assumed that, during the penetration process, the target material undergoes only axisymmetric deformation perpendicular to the penetration direction, with no deformation occurring parallel to it. As shown in Figure 1, the radius of the cylindrical target without expansion is r_{t0}, the target at time t is r_t, the cavity radius is r_c, and the elastic–plastic interface radius is r_p. As the cavity radius expands to r_{c1}, the elastic–plastic boundary reaches the target lateral boundary. When the cavity radius expands to r_{c2}, the target fractures. Therefore, the process of cavity expansion can be divided into two stages based on the cavity radius. The first stage is the elastic–plastic stage ($r_c < r_{c1}$), which is composed of the cavity region ($0 < r < r_c$), the plastic region ($r_c < r < r_p$), and the elastic region ($r_p < r < r_t$). The second stage is the plastic stage ($r_{c1} < r_c < r_{c2}$), which is composed of the cavity region ($0 < r < r_c$) and the plastic region ($r_c < r < r_t$), where r is the radial coordinate in the Euler coordinate (positive outward).

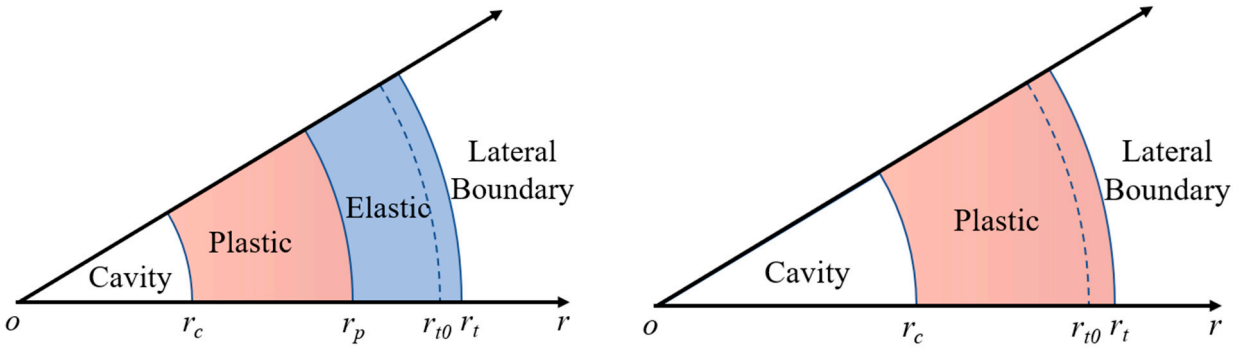


Figure 1. Schematic diagram of quasi-static finite cylindrical cavity expansion model: (**a**) elastic–plastic stage; (**b**) plastic stage.

Based on the axisymmetric assumption, the momentum conservation equation in Euler coordinates is

$$\frac{d\sigma_r}{dr} + \frac{\sigma_r - \sigma_\theta}{r} = 0, \tag{1}$$

where σ_r and σ_θ are the radial and hoop components, respectively, of Cauchy stress taken to be positive under compression.

To obtain a relatively precise analytical solution, it is assumed that the target behaves as an elastic, perfectly plastic rate-independent material according to [15,27]. The target material in the elastic region is assumed to obey Hooke's law. The stress–displacement relations based on the axisymmetric assumption and Hooke's law are as follows:

$$\sigma_r = -\frac{E}{(1+v)(1-2v)}\left[(1-v)\frac{du}{dr} + v\frac{u}{r}\right], \tag{2}$$

$$\sigma_\theta = -\frac{E}{(1+v)(1-2v)}\left[v\frac{du}{dr} + (1-v)\frac{u}{r}\right], \tag{3}$$

where Y_t is the flow stress of the target, E is Young's modulus of the target material, v is Poisson's ratio, and u is the radial displacement (positive outward).

And the unified yield criterion of metal materials under axisymmetric conditions [22] is employed to describe the target material in the plastic region and investigate the resistance characteristics of the target under different yield conditions:

$$\sigma_r - \sigma_\theta = \frac{2(1+b)}{2+b}Y_t, \tag{4}$$

where Y_t is the flow stress of the target and b ($0 < b < 1$) is the yield criterion coefficient. When b is set to 0, 0.367, and 1, the Tresca yield criterion, Mises yield criterion, and twin shear yield criterion are used, respectively.

2.2. Analytical Solution for Cavity Pressure

2.2.1. Elastic–Plastic Response Stage ($r_c < r_{c1}$)

- Elastic region ($r_p < r < r_t$)

  With (2) and (3), (1) transforms to

$$\frac{d^2u}{dr^2} + \frac{1}{r}\frac{du}{dr} - \frac{u}{r^2} = 0. \tag{5}$$

Since σ_r at the lateral boundary of the target is 0 and Equation (4) holds at the elastic–plastic interface, integration gives

$$u(r) = \frac{(1+b)(1+v)Y_t}{(2+b)E}\left[\frac{r_p^2}{r} + (1-2v)\frac{r_p^2}{r_t^2}r\right], \tag{6}$$

$$\sigma_r(r) = \frac{(1+b)Y_t}{(2+b)}\left(\frac{r_p^2}{r^2} - \frac{r_p^2}{r_t^2}\right). \tag{7}$$

- Plastic region ($r_c < r < r_p$)

  Substituting Equation (4) into Equation (1) yields

$$\frac{d\sigma_r}{dr} + \frac{2(1+b)Y_t}{(2+b)r} = 0, \tag{8}$$

and integration gives

$$\sigma_r(r) = \frac{(1+b)Y_t}{(2+b)}\left(1 - \frac{r_p^2}{r_t^2} + \ln\frac{r_p^2}{r^2}\right), \tag{9}$$

- Interface Conditions

  Assuming that the plastic region is incompressible, it can be concluded that

$$r_p^2 - r_c^2 = \left(r_p - u(r_p)\right)^2. \tag{10}$$

  Substituting Equation (6) into Equation (10) yields

$$r_c^2 + D^2\left[r_p^2 + 2(1-2v)\frac{r_p^4}{r_t^2} + (1-2v)^2\frac{r_p^6}{r_t^4}\right] = 2D(1-2v)\frac{r_p^4}{r_t^2} + 2Dr_p^2, \tag{11}$$

$$D = \frac{(1+b)(1+v)Y_t}{(2+b)E}. \tag{12}$$

  With $u(r_t) = r_t - r_{t0}$, (6) transforms to

$$\frac{2(1+b)(1-v^2)Y_t}{(2+b)E}r_p^2 = r_t^2 - r_{t0}r_t. \tag{13}$$

If $r_c = r_{c1}$, then $r_p = r_t$. From (10), and ignoring higher order terms in $u(r_p)$ according to [28],

$$r_{c1}^2 = 2u(r_{t1})r_{t1}, \tag{14}$$

where r_{t1} is the target radius if $r_c = r_{c1}$. From (6), (13), and (14), r_{c1} can be obtained

$$r_{c1} = \frac{2\sqrt{(1+b)(2+b)(1-v^2)EY_t}}{(2+b)E - 2(1+b)(1-v^2)Y_t}r_{t0}. \tag{15}$$

2.2.2. Plastic Response Stage ($r_{c1} < r_c < r_{c2}$)

With the lateral boundary conditions, integration of (8) gives

$$\sigma_r(r) = \frac{(1+b)Y_t}{(2+b)}\ln\frac{r_t^2}{r^2}. \tag{16}$$

It can be concluded from (10) that

$$r_t^2 = r_{t0}^2 + r_c^2. \tag{17}$$

Substituting Equation (17) into Equation (16) yields

$$\sigma_r(r) = \frac{(1+b)Y_t}{(2+b)} \ln\left(\frac{r_{t0}^2 + r_c^2}{r^2}\right). \tag{18}$$

r_{c2} can be taken as [26]

$$r_{c2} = r_t \sqrt{\frac{(2+b)\varepsilon_f}{1+b}}, \tag{19}$$

where ε_f is the uniaxial ultimate strain. Substituting Equation (17) into Equation (19) gives r_{c2} considering the deformation of the target:

$$r_{c2} = \frac{\sqrt{\frac{(2+b)\varepsilon_f}{1+b}}}{\sqrt{1 - \frac{(2+b)\varepsilon_f}{1+b}}} r_{t0}. \tag{20}$$

2.2.3. Semi-Infinite Target

For a semi-infinite target ($r_t \to \infty$), σ_r can be obtained from Equations (9) and (11):

$$\sigma_r(r) = \frac{(1+b)Y_t}{(2+b)} \left\{1 + \ln \frac{r_c^2}{r^2} \left[\frac{(2+b)^2 E^2}{2(1+b)(2+b)(1+v)EY_t - ((1+b)(1+v)Y_t)^2}\right]\right\}. \tag{21}$$

In summary, the cavity stress at each stage for the finite target and the semi-infinite target is

$$\sigma_{rc} = \begin{cases} \frac{(1+b)Y_t}{(2+b)}\left(1 - \frac{r_p^2}{r_t^2} + \ln \frac{r_p^2}{r_c^2}\right), r_c < r_{c1} \\ \frac{(1+b)Y_t}{(2+b)} \ln\left(1 + \frac{r_{t0}^2}{r_c^2}\right), r_{c1} \le r_c \le r_{c2} \\ 0, r_c \ge r_{c2} \\ \frac{(1+b)Y_t}{(2+b)}\left\{1 + \ln \frac{r_c^2}{r^2}\left[\frac{(2+b)^2E^2}{2(1+b)(2+b)(1+v)EY_t - ((1+b)(1+v)Y_t)^2}\right]\right\}, r_t \to \infty \end{cases}. \tag{22}$$

where σ_{rc} is the radial stress at the cavity.

2.3. Average Cavity Pressure and the Decay Function for the Lateral Boundary Effect

The energy dissipated during the expansion of the cavity radius from 0 to the final value r_{cf} is equal to the work performed by the cavity pressure [25]. Therefore, the energy dissipated per unit thickness is

$$W_e = \int_0^{r_{cf}} (2\pi r_c \sigma_{rc}) dr_c = 2\pi \int_0^{r_{cf}} \sigma_{rc} r_c dr_c, \tag{23}$$

assuming that the work performed by the average pressure of the cavity $\overline{\sigma}_{rc}$ on the displacement of the expansion is equal to the energy dissipated of the expansion, $\overline{\sigma}_{rc}$ can be obtained from the conservation of energy as follows:

$$\overline{\sigma}_{rc} = \frac{W_e}{\pi r_{cf}^2} = \frac{\int_0^{r_{cf}} \sigma_{rc} r_c dr_c}{\frac{1}{2} r_{cf}^2}. \tag{24}$$

With (22) and (24), the decay function for the lateral boundary effect can be given as follows:

$$f\left(r_{cf}, r_{t0}\right) = \frac{\overline{\sigma}_{rc}}{\sigma_{rc}|_{r_t \to \infty}}. \tag{25}$$

3. Theoretical Penetration Model and Model Verification

In this section, a modified Alekseevskii–Tate model based on the decay function for the lateral boundary effect is developed. Analytical solutions for the penetration depth are obtained. The penetration depth results from existing experiments and numerical simulations are subsequently used to validate the proposed model.

3.1. Modified Alekseevskii–Tate Model and Calculation of Penetration Depth

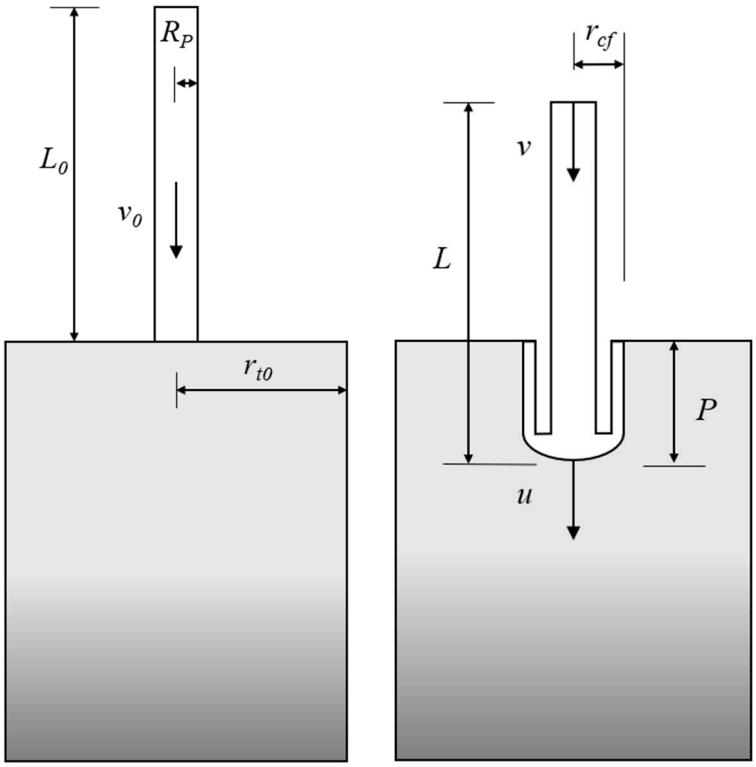
According to Tate [5,6], it is assumed that the interface of the high-velocity long-rod and the target is semi-fluid and the initial shape of the long-rod's nose has negligible effects on the penetration depth. As shown in Figure 2, R_P is the radius of the rod; v_0 and L_0 are the initial impact velocity and the initial length of the projectile, respectively; and u, v, P, and L are the penetration velocity, tail velocity, penetration depth, and remaining length of the rod, respectively. The following basic equations can be drawn according to the Alekseevskii–Tate model [5]:

$$\frac{1}{2}\rho_P(v-u)^2 + Y_P = \frac{1}{2}\rho_T u^2 + R_T, \tag{26}$$

$$\frac{dl}{dt} = -(v-u), \tag{27}$$

$$\frac{dP}{dt} = u, \tag{28}$$

$$\frac{dv}{dt} = -\frac{Y_P}{\rho_P L}. \tag{29}$$



(**a**) (**b**)

Figure 2. Schematic diagram of long-rod and cylindrical metal thick target with finite diameter: (**a**) before impact; (**b**) shortly after impact.

The initial conditions are as follows:

$$P(0) = 0, L(0) = L_0, v(0) = v_0, \tag{30}$$

where ρ_P and ρ_T are the density of the rod and target, respectively; Y_P is the dynamic flow stress of the rod; and R_T is the target resistance.

Y_P can be taken as [29]

$$Y_P = (1 + \lambda)\sigma_{\mathrm{yp}}. \tag{31}$$

By using (25), R_T can be modified as

$$R_T = f\left(r_{cf}, r_{t0}\right) R_T^*, \tag{32}$$

$$R_T^* = Y_t\left(\frac{2}{3} + \ln\frac{2E}{(4 - e^{-\lambda})Y_t}\right), \tag{33}$$

where σ_{yp} is the yield stress of the rod; λ is usually taken as 0.7; R_t* is the target resistance of a semi-infinite target [29]; and r_{cf} can be taken as the channel radius [8]:

$$r_{cf} = R_P\left(1 + 0.287v_0 + 0.148v_0^2\right), \tag{34}$$

where v_0 is measured in km/s.

Using the above equations, the depth of penetration can be calculated in two situations determined by the relationship between Y_P and R_t.

- $Y_P < R_t$

In this situation, the long-rod only undergoes eroding penetration. When $v = v_{\mathrm{c}}$ and $u = 0$ are reached, the penetration ends, and the remaining long-rod continues to erode until the residual velocity reaches 0. The penetration depth can be obtained as follows:

$$P = \frac{\rho_P L_0}{Y_P}\int_{v_c}^{v_0}\frac{1}{1-\lambda^2}\left(v - \lambda\sqrt{v^2 + A}\right)\left(\frac{v(v)}{v(v_0)}\right)^{k_1}\exp\{k_2[\vartheta(v) - \vartheta(v_0)]\}\mathrm{d}v, \tag{35}$$

$$v_c = \sqrt{\frac{2(R_T - Y_P)}{\rho_P}}, \lambda = \sqrt{\frac{\rho_T}{\rho_P}}, A = \frac{2(R_T - Y_P)}{\rho_T}\left(1 - \lambda^2\right), \tag{36}$$

$$v(x) = x + \sqrt{x^2 + A}, \vartheta(x) = x\sqrt{x^2 + A} - \lambda x^2, \tag{37}$$

$$k_1 = \frac{R_T - Y_P}{\lambda Y_P}, k_2 = \frac{\lambda\rho_P}{2(1-\lambda^2)Y_P}. \tag{38}$$

- $Y_P > R_t$

In this situation, the penetration depth can be divided into two parts: eroding penetration and rigid body penetration. First, the high-speed long-rod undergoes eroding penetration until the penetration speed is equal to the tail velocity ($u = v = v_r$). Then, the remaining long-rod (with remaining length L_{r}) penetrates as a rigid body at the remaining velocity v_{r}. The depth of penetration can therefore be obtained as

$$P_1 = \frac{\rho_P L_0}{Y_P}\int_{v_r}^{v_0}\frac{1}{1-\mu^2}\left(v - \mu\sqrt{v^2 + A}\right)\left(\frac{v(v)}{v(v_0)}\right)^{k_1}\exp\{k_2[\vartheta(v) - \vartheta(v_0)]\}\mathrm{d}v, \tag{39}$$

$$v_r = \sqrt{\frac{2(Y_P - R_T)}{\rho_T}}, \tag{40}$$

$$P_2 = \frac{\rho_P L_r R_P^2 v_r^2}{2 r_{cf}^2 R_T}, \tag{41}$$

$$r_{cf} = R_P\left(1 + 0.287 v_0 + 0.148 v_0^2\right), \tag{42}$$

$$L_r = L_0\left(\frac{v(v_r)}{v(v_0)}\right)^{k_1} \exp[k_2(\vartheta(v_r) - \vartheta(v_0))], \tag{43}$$

$$P = P_1 + P_2. \tag{44}$$

3.2. Validation of the Theoretical Model

In Section 3.2, b = 0.367, i.e., the Mises yield criterion, is used in the proposed model. Experiments on long rods with different initial impact velocities penetrating metal targets with different diameters were carried out in [23,24]. The mechanical parameters of the rod and target materials are summarized in Table 1. As the flow stress is not always given, it can be estimated from the Brinell hardness [30]:

$$\sigma_y = 3.92 \times \mathrm{BHN}, \tag{45}$$

where σ_y is the flow stress, in MPa; BHN is the Brinell hardness.

Table 1. Mechanical parameters of long-rod and target material in references.

Reference	σ_{yp} (MPa)	Y_t (MPa)	ρ_P (kg/m^3)	ρ_T (kg/m^3)	L_0 (mm)	R_P (mm)
Littlefield et al. [23]	1300	1055 [1]	17,730	7850	77.9	3.895
Forrestal et al. [24]	1140 [13]	400 [13]	7830	2710	74.655	3.555

[1] Calculated using Equation (45).

It is clear from the figure in [23] that the target undergoes significant radial expansion after penetration, which is consistent with the model in this article. In addition, numerical simulation calculations show that the elastic–plastic interface just reaches the lateral boundary of the target when r_{t0}/R_P is approximately 15 [23], while the theoretical model in this paper and other references predicts that the elastic–plastic interface reaches the lateral boundary of the target when r_{t0}/R_P = 16.63, 19.92 [23], 19.3 [25], and 17.4 [26]. The proposed model is closest to the numerical simulation results.

Figure 3 shows the comparison of experimental and numerical results [23] with the calculation results of penetration depths for different r_{t0}/R_P. Tables 2 and 3 summarize the initial penetration conditions, penetration depth results, and predicted penetration depths of different theoretical models in [23,24], respectively. From Figure 3 and Table 2, the following conclusions can be drawn:

- The proposed model is in good agreement with the experimental and numerical results, while all the other theoretical models overestimate the penetration depth;
- Although Wang's [26] model has better prediction results than Jiang's [25] and Littlefield's [23] models, there is a sudden change in the penetration depth when r_{t0}/R_P is around 18.5, which will result in multiple results within a certain range of r_{t0}/R_P.

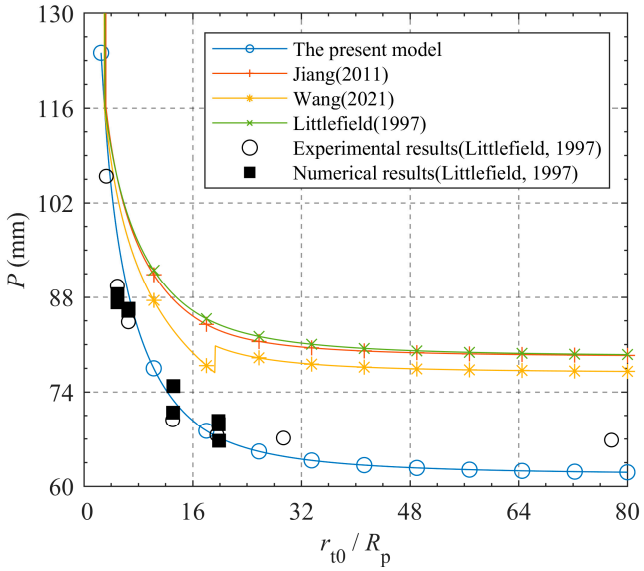


Figure 3. Comparison of calculation results of penetration depths using the model in [23,25,26] and in this article with experimental and numerical results in [23].

Table 2. Summary of initial penetration conditions, penetration depths, and calculation results of different theoretical model [23].

Resource	v_0 (m/s)	r_{t0}/R_P	P_e (mm) *	P_{max} (mm)	P_{max2} [25] (mm)	P_{max3} [26] (mm)	P_{max4} [23] (mm)
Experimental results [23]	1500	4.90	87.25	97.14	105.59	102.96	105.65
	1500	4.90	88.49	97.14	105.59	102.96	105.65
	1500	6.53	86.31	88.47	99.49	96.49	99.90
	1500	6.52	86.00	88.51	99.52	96.52	99.93
	1500	13.10	70.97	72.83	87.72	83.14	88.47
	1500	13.12	74.86	72.81	87.70	83.12	88.45
	1500	19.83	69.25	67.23	83.11	80.60	83.97
	1500	19.79	69.72	67.25	83.13	80.62	83.98
	1500	19.88	66.76	67.20	83.09	80.58	83.95
Numerical results [23]	1500	3.26	105.94	112.38	115.69	113.51	114.64
	1500	4.89	89.66	97.20	105.64	103.01	105.69
	1500	6.52	84.37	88.51	99.52	96.52	99.93
	1500	13.04	69.88	72.91	87.78	83.22	88.53
	1500	19.56	67.62	67.36	83.22	80.71	84.08
	1500	29.34	67.15	64.43	80.94	78.52	81.57
	1500	77.66	66.84	62.10	79.42	77.06	79.55

* P_e are the experimental and numerical results of penetration depth in [23]; P_{max}, P_{max2}, P_{max3}, and P_{max4} are penetration depths calculated by the proposed model and the models in [23,25,26], respectively.

Let the ratio of the resistance of a finite-diameter target to the resistance of a semi-infinite target R_T/R_T^* be the normalized target resistance. Figure 4 shows the comparison of the calculated normalized target resistance with the numerical results [24]. From Figure 4, the following can be concluded:

- The proposed model is in good agreement with the numerical results. The calculated results are smaller than the numerical results when $r_{t0}/R_P > 6.5$. The reason is that the model does not consider the propagation time of elastic waves during the elastic–plastic stage;
- Due to the assumption that the target material is incompressible during the plastic stage, the target resistance is overestimated when $r_{t0}/R_P < 6.5$ compared to the numerical results.

Table 3. Summary of initial penetration conditions, penetration depths, and calculation results of different theoretical models [24].

v_0 (m/s)	r_{t0}/R_P	P_e (mm) *	P_{max} (mm)	P_{max2} [25] (mm)	P_{max3} [26] (mm)	P_{max4} [23] (mm)
1037	35.16	64.6	57.44	116.52	115.53	117.07
1042	35.16	41.6	57.90	117.17	116.17	117.72
1174	35.16	67.5	69.61	133.54	132.40	134.11
1174	35.16	66.5	69.61	133.54	132.40	134.11
1193	35.16	50.7	71.22	135.77	134.61	136.33
1216	35.16	50.7	73.14	138.42	137.24	138.98
1284	35.16	78.8	78.61	145.94	144.70	146.49
1337	35.16	61.8	82.64	151.48	150.19	152.01
1411	35.16	106.1	87.91	158.73	157.38	159.23
1515	35.16	76	94.58	167.96	166.53	168.40
1802	35.16	94.3	108.50	187.81	186.20	187.97
1813	35.16	120	108.92	188.41	186.80	188.56
2052	35.16	113.9	116.01	199.00	197.29	198.80
2204	35.16	124.6	119.00	203.43	201.68	202.96
2255	35.16	137.4	119.80	204.57	202.81	204.00
2476	35.16	137.9	122.34	207.70	205.92	206.66

* P_e are the experimental results of penetration depth in [24]; P_{max}, P_{max2}, P_{max3}, and P_{max4} are penetration depths calculated by the proposed model and the models in [23,25,26], respectively.

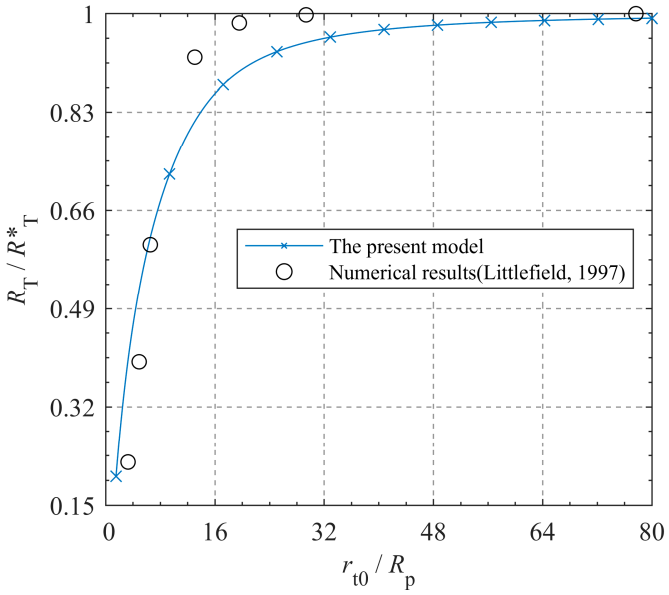


Figure 4. Comparison of results of the normalized target resistance with numerical results in [23].

The comparison of the calculation results of penetration depths with experimental results [24] for different initial impact velocities is shown in Figure 5. From Figure 5, the following can be concluded:

- The proposed model is in good agreement with the experimental results. The calculation results of the proposed model continue to increase and tend towards the fluid dynamic limit as the initial impact velocity increases;
- The calculation results of the other three models are all significantly greater than the experimental results because the R_T predicted by the three models is less than Y_P. When the penetration velocity is less than $v_r \approx 2500$ m/s, there is only a rigid body penetration phase. However, when the initial impact velocity is greater than v_r, the penetration process exhibits an eroding penetration stage. The calculation results of the three models rapidly decrease and tend towards the fluid dynamic limit.

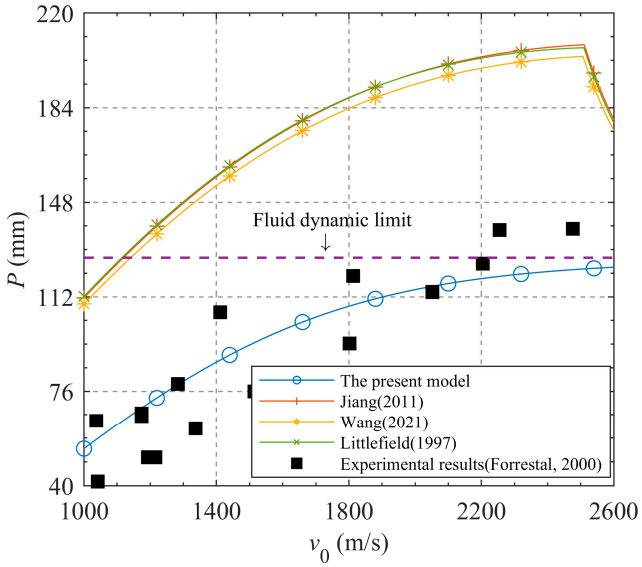


Figure 5. Comparison of calculation results of penetration depths using the model in [23,25,26] and in this article with existing experimental results in [24].

Table 4 shows the mean percentage error, root mean square error, and mean absolute error of the theoretical models. The results show that the proposed model has higher accuracy and better applicability.

Table 4. Summary of statistical errors.

Method	Statistical Error	Experimental Results [23]	Numerical Results [23]	Experimental Results [24]
The present model	MPE *	2.29%	1.75%	9.47%
	RMSE	3.56	4.12	11.78
	MAE	0.06	0.06	0.22
Jiang [25]	MPE	19.53%	19.01%	94.73%
	RMSE	15.03	14.39	71.60
	MAE	0.20	0.20	1.07
Wang [26]	MPE	15.48%	15.30%	93.12%
	RMSE	11.93	11.59	70.28
	MAE	0.16	0.16	1.06
Littlefield [23]	MPE	20.30%	19.44%	95.13%
	RMSE	15.59	14.65	71.78
	MAE	0.21	0.20	1.08

* MPE, RMSE, and MAE are mean percentage error, root mean square error, and mean absolute error, respectively.

4. Results and Discussions

In this section, the effects of the target diameter, initial impact velocity, and yield criterion are investigated based on the material parameters in [23].

4.1. Effect of Target Diameter

Figure 6 shows the comparison of normalized target resistance and penetration depth with r_{t0}/R_P at initial impact velocities of 1000 m/s, 1500 m/s, and 2000 m/s. Figure 7 shows the comparison of penetration velocity and tail velocity with penetration depth at different r_{t0}/R_P values of 5, 10, and 20. From Figures 6 and 7, the following can be seen:

- When $r_{t0}/R_P < 25$, R_t/R_t^* decreases rapidly as r_{t0}/R_P decreases, while R_t/R_t^* decreases slowly as r_{t0}/R_P decreases when $r_{t0}/R_P > 25$. This suggests that R_t/R_t^* rapidly decreases as the elastic–plastic interface approaches the target boundary ($r_{t0}/R_P = 16.63$).

- When $r_{t0}/R_P < 25$, the penetration depth increases exponentially with decreasing r_{t0}/R_P. However, when $r_{t0}/R_P > 25$, the penetration depth slowly increases with decreasing r_{t0}/R_P. This is because of the decrease in R_t/R_t*. When $r_{t0}/R_P = 25$, the deviation of the penetration depth from the semi-infinite target is less than 10%, which means that the target can be treated as a semi-infinite target when $r_{t0}/R_P > 25$.
- As the circumferential constraint effect decreases, the initial penetration velocity and penetration depth gradually increase.

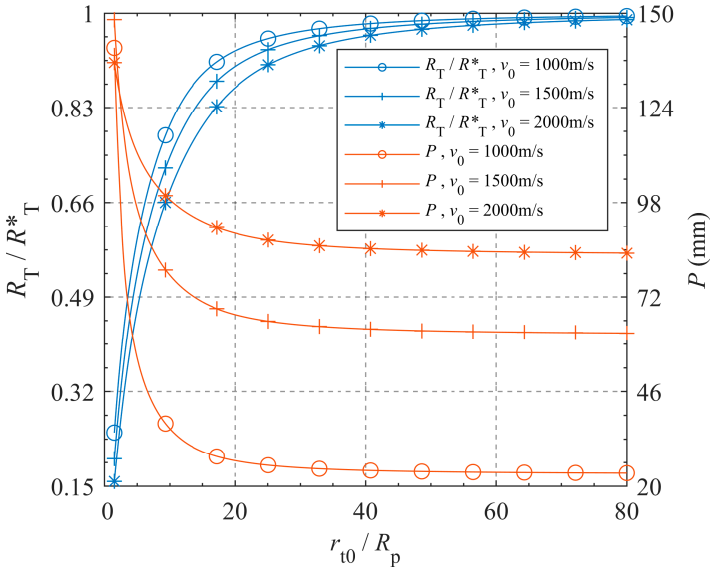


Figure 6. Comparison of normalized target resistance and penetration depth with r_{t0}/R_P.

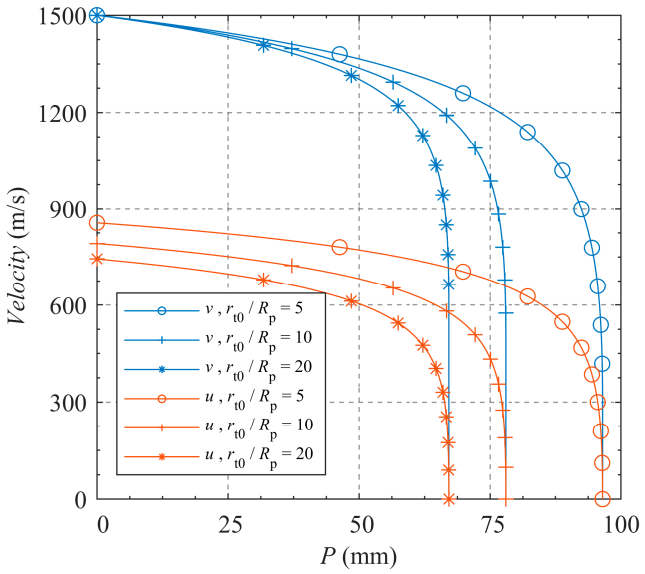


Figure 7. Comparison of penetration velocity and tail velocity with penetration depth of different r_{t0}/R_P.

Figure 8 compares the decay functions of the target resistance in this article with those in [17]. As shown in Figure 8, the lateral boundary effect in the elastic–plastic stage is relatively small. When the elastic–plastic interface approaches the lateral boundary, the target resistance decreases by about 13%. Different from the decay functions in [17], the following can be seen:

- Because the proposed decay function is based on the average cavity pressure rather than the instantaneous cavity pressure, the proposed decay function decreases more slowly than that in [17];
- The diameter of the target is greater as the elastic–plastic interface intersects the target boundary in the proposed decay function because of the use of the finite cylindrical cavity expansion model;
- The proposed decay function will not decrease to 0 before the initial target radius decreases to 0. The reason for this is that the target deformation is taken into account in this article;
- Due to the fact that the target resistance of long-rod penetration is independent of velocity, the decay function in this article is independent of velocity, whereas the decay function in [17] decreases significantly with increasing velocity.

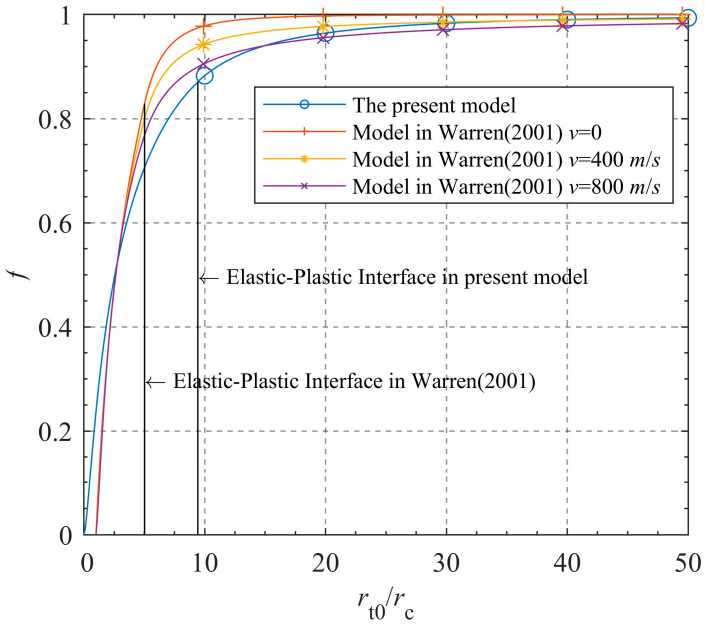


Figure 8. Decay functions in this article and [17] vs. r_{t0}/r_c.

4.2. Effect of Initial Impact Velocity

Figure 9 shows the comparison of normalized target resistance and penetration depth with initial impact velocity at r_{t0}/R_P values of 5, 10, and 20. Figure 10 shows the comparison of penetration velocity and tail velocity with penetration depth at initial impact velocities of 1000 m/s, 1500 m/s, and 2000 m/s. From Figures 9 and 10, the following can be seen:

- The penetration depth increases with increasing initial impact velocity and gradually approaches the fluid dynamic limit. In the case of $r_{t0}/R_P = 5$, when the initial impact velocity is greater than 2500 m/s, the penetration depth will be slightly greater than the fluid dynamic limit. This is because when $v_0 > 2500$ m/s at $r_{t0}/R_P = 5$, R_T is less than Y_P, and rigid penetration occurs during the penetration process;
- R_t/R_t^* decreases approximately linearly as the initial impact velocity increases. This is because r_{cf} increases as the initial impact velocity increases, leading to an increase in the lateral boundary effect;
- Both the initial penetration velocity and penetration depth increase significantly as the initial impact velocity increases.

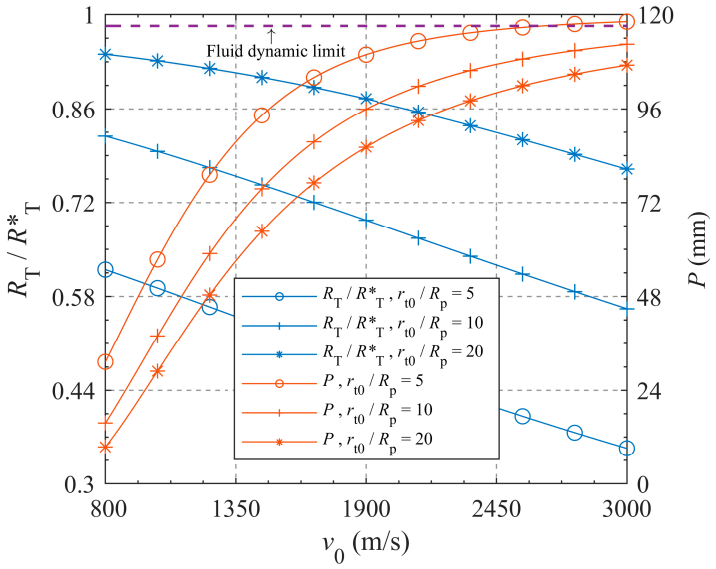


Figure 9. Comparison of normalized target resistance and penetration depth with initial impact velocity.

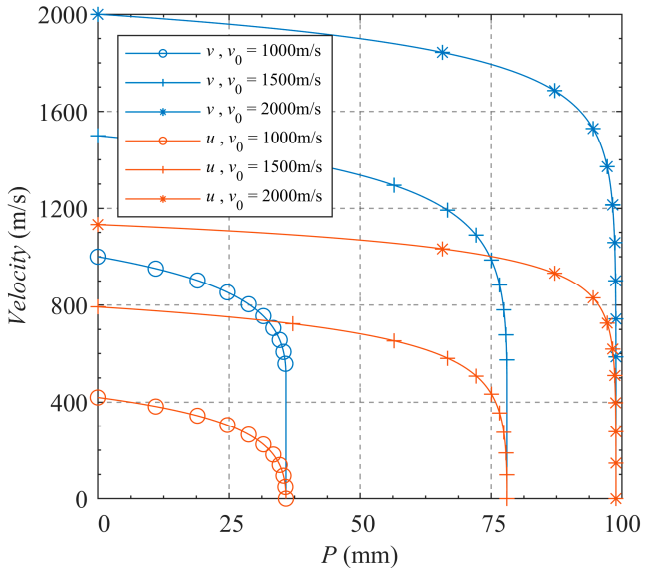
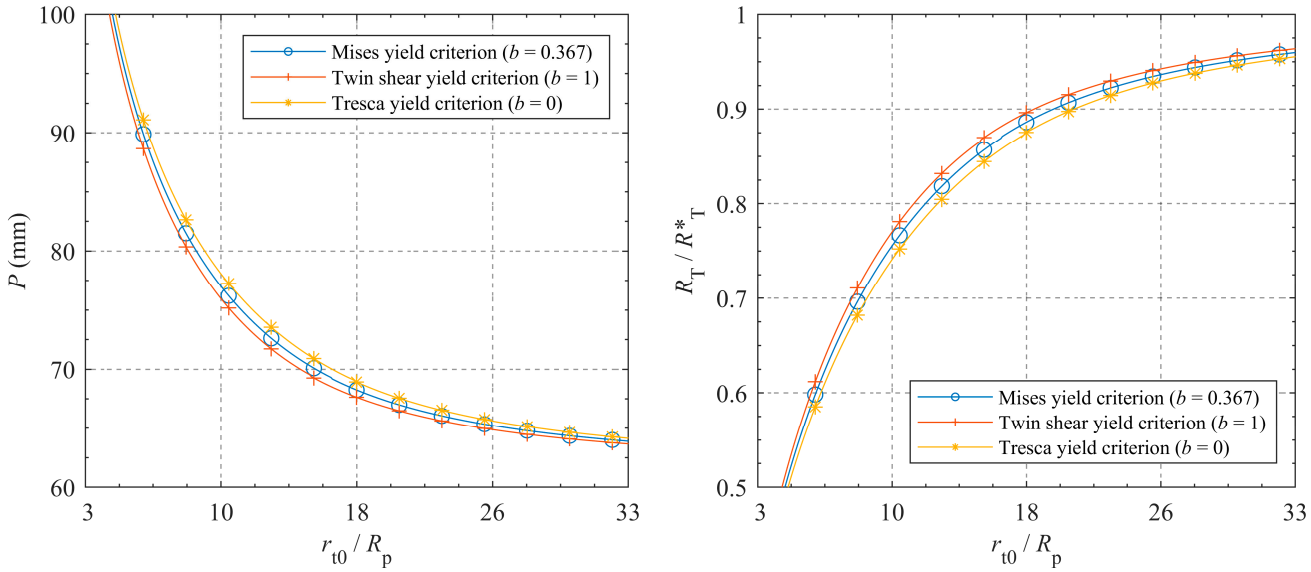


Figure 10. Comparison of penetration velocity and tail velocity with penetration depth of different initial impact velocities.

4.3. Effect of Yield Criteria

With different b values, different yield criteria can be applied in the proposed model. Figure 11 shows the variation in penetration depth and normalized target resistance with r_{t0}/R_P when the Tresca yield criterion (b = 0), twin shear yield criterion (b = 1), and Mises yield criterion (b = 0.367) are used, respectively. Table 5 shows the ranges of penetration depth and normalized target resistance at different r_{t0}/R_P. Figure 11 and Table 5 show the following:

- As b increases, the penetration depth decreases and R_t/R_t^* increases slightly;
- The calculated penetration depth and target resistance are less affected by the yield criterion. For different yield criteria, the maximum deviations in the penetration depth and penetration resistance are 2.36% and 4.62%, respectively. The reason is that the R_t^* used in this model is independent of the yield criterion.



(**a**) (**b**)

Figure 11. Comparison of penetration depth and normalized target resistance of different yield criteria: (**a**) penetration depth; (**b**) normalized target resistance.

Table 5. Summary of penetration depth and normalized target resistance ranges.

r_{t0}/R_P	Range of Penetration Depths (mm)	Range of R_t/R_t*
3	114.74~117.44	0.368~0.386
5	95.20~97.74	0.519~0.543
7	85.37~87.77	0.622~0.649
9	79.23~81.48	0.697~0.726
11	75.04~77.11	0.754~0.783
13	72.05~73.91	0.799~0.827
15	69.89~71.52	0.835~0.860
17	68.24~69.71	0.863~0.886
19	67.09~68.27	0.886~0.905
21	66.21~67.23	0.903~0.920
30	64.05~64.62	0.947~0.957
80	62.04~62.12	0.991~0.993

5. Summary and Conclusions

In summary, a theoretical model of high-speed penetration of finite-diameter metal targets by a long-rod is established using a quasi-static finite cylindrical cavity expansion model. The calculated results are in good agreement with the experimental results. Studies have also been conducted on the factors influencing the long-rod penetration into metal targets with finite diameters. The conclusions are as follows:

- The proposed model requires only the material and size parameters of the target and the long-rod as inputs, and predicts the penetration depth well across a range of r_{t0}/R_P, varying target and long-rod materials, and diverse v_0;
- The penetration depth increases by less than 10% between semi-infinite targets and r_{t0}/R_P = 25. However, an increase of more than 50% in the penetration depth occurs between r_{t0}/R_P = 25 and r_{t0}/R_P = 5. Therefore, the lateral boundary effect should be taken into account when r_{t0}/R_P < 25;
- The penetration depth increases dramatically with increasing v_0 before the fluid dynamic limit. On the other hand, R_t decreases significantly with v_0 due to the increase in the channel radius caused by v_0. Therefore, the lateral boundary effect is also influenced by v_0;

- The penetration depth decreases very little as b increases, which indicates that the yield criterion has little effect on the lateral boundary effect and R_t.

Author Contributions: Conceptualization, Y.L. and X.T.; methodology, Y.L.; software, Y.L.; validation, Y.L. and J.S.; formal analysis, Y.L.; investigation, Y.L. and B.Z.; resources, X.T.; data curation, Y.L., X.X. and J.S.; writing—original draft preparation, Y.L.; writing—review and editing, X.T., Y.C. and B.Z.; visualization, Y.L., X.X. and J.W.; supervision, X.T.; funding acquisition, X.T. All authors have read and agreed to the published version of the manuscript.

Funding: This research received no external funding.

Institutional Review Board Statement: Not applicable.

Informed Consent Statement: Not applicable.

Data Availability Statement: Data are contained within the article.

Acknowledgments: Yunke Lu would like to extend his sincere gratitude to Cong Sun for her invaluable support.

Conflicts of Interest: The authors declare no conflicts of interest.

References

1. Orphal, D.L. Explosions and Impacts. *Int. J. Impact Eng.* **2006**, *33*, 496–545. [CrossRef]
2. Rosenberg, Z.; Dekel, E. *Terminal Ballistics*; Springer: Singapore, 2016; pp. 1–76. ISBN 978-981-10-0393-6.
3. Anderson, C.E., Jr. Analytical Models for Penetration Mechanics: A Review. *Int. J. Impact Eng.* **2017**, *108*, 3–26. [CrossRef]
4. Alekseevskii, V.P. Penetration of a Rod into a Target at High Velocity. *Combust. Explos. Shock Waves* **1966**, *2*, 63–66. [CrossRef]
5. Tate, A. A Theory for the Deceleration of Long Rods after Impact. *J. Mech. Phys. Solids* **1967**, *15*, 387–399. [CrossRef]
6. Tate, A. Further Results in the Theory of Long Rod Penetration. *J. Mech. Phys. Solids* **1969**, *17*, 141–150. [CrossRef]
7. Rosenberg, Z.; Marmor, E.; Mayseless, M. On the Hydrodynamic Theory of Long-Rod Penetration. *Int. J. Impact Eng.* **1990**, *10*, 483–486. [CrossRef]
8. Walker, J.D.; Anderson, C.E. A Time-Dependent Model for Long-Rod Penetration. *Int. J. Impact Eng.* **1995**, *16*, 19–48. [CrossRef]
9. Zhang, L.S.; Huang, F.L. Model for Long-Rod Penetration into Semi-Infinite Targets. *J. Beijing Inst. Technol.* **2004**, *13*, 285–289. [CrossRef]
10. Lan, B.; Wen, H. Alekseevskii-Tate Revisited: An Extension to the Modified Hydrodynamic Theory of Long Rod Penetration. *Sci. China Technol. Sci.* **2010**, *53*, 1364–1373. [CrossRef]
11. Kong, X.Z.; Wu, H.; Fang, Q.; Peng, Y. Rigid and Eroding Projectile Penetration into Concrete Targets Based on an Extended Dynamic Cavity Expansion Model. *Int. J. Impact Eng.* **2017**, *100*, 13–22. [CrossRef]
12. Bishop, R.F.; Hill, R.; Mott, N.F. The Theory of Indentation and Hardness Tests. *Proc. Phys. Soc.* **1945**, *57*, 147. [CrossRef]
13. Warren, T.L.; Forrestal, M.J. Effects of Strain Hardening and Strain-Rate Sensitivity on the Penetration of Aluminum Targets with Spherical-Nosed Rods. *Int. J. Solids Struct.* **1998**, *35*, 3737–3753. [CrossRef]
14. Forrestal, M.J.; Tzou, D.Y. A Spherical Cavity-Expansion Penetration Model for Concrete Targets. *Int. J. Solids Struct.* **1997**, *34*, 4127–4146. [CrossRef]
15. Chen, X.W.; Li, Q.M. Deep Penetration of a Non-Deformable Projectile with Different Geometrical Characteristics. *Int. J. Impact Eng.* **2002**, *27*, 619–637. [CrossRef]
16. Macek, R.W.; Duffey, T.A. Finite Cavity Expansion Method for Near-Surface Effects and Layering during Earth Penetration. *Int. J. Impact Eng.* **2000**, *24*, 239–258. [CrossRef]
17. Warren, T.L.; Poormon, K.L. Penetration of 6061-T6511 Aluminum Targets by Ogive-Nosed VAR 4340 Steel Projectiles at Oblique Angles: Experiments and Simulations. *Int. J. Impact Eng.* **2001**, *25*, 993–1022. [CrossRef]
18. Warren, T.L.; Hanchak, S.J.; Poormon, K.L. Penetration of Limestone Targets by Ogive-Nosed VAR 4340 Steel Projectiles at Oblique Angles: Experiments and Simulations. *Int. J. Impact Eng.* **2004**, *30*, 1307–1331. [CrossRef]
19. Chen, X.; Lu, F.; Zhang, D. Penetration Trajectory of Concrete Targets by Ogived Steel Projectiles–Experiments and Simulations. *Int. J. Impact Eng.* **2018**, *120*, 202–213. [CrossRef]
20. Wei, H.; Liu, J.; Zhang, X.; Liu, C.; Li, P.; Qiao, L. Study on Perforation of Elliptical Cross-Section Projectile into Finite-Thick Metal Targets. *Acta Mech. Sin.* **2023**, *39*, 422429. [CrossRef]
21. Song, D.; Liu, F.; Jiang, Z. Prediction of Projectile an Analytical Model for Penetration into Cylindrical Metallic Thick Target by Rigid Sharp-Nosed Projectiles. *Eng. Mech.* **2013**, *30*, 31–36. (In Chinese) [CrossRef]
22. Wang, J.; Zhao, J.; Zhou, Y.; Sun, S. Boundary Effect and Dynamic Response Study for the Penetration of Rigid Projectiles into Thick, Finite-Radius, Metallic Targets. *Shock Vib.* **2020**, *2020*, e8832925. [CrossRef]
23. Littlefield, D.L.; Anderson, C.E.; Partom, Y.; Bless, S.J. The Penetration of Steel Targets Finite in Radial Extent. *Int. J. Impact Eng.* **1997**, *19*, 49–62. [CrossRef]

24. Forrestal, M.J.; Piekutowski, A.J. Penetration Experiments with 6061-T6511 Aluminum Targets and Spherical-Nose Steel Projectiles at Striking Velocities between 0.5 and 3.0km/s. *Int. J. Impact Eng.* **2000**, *24*, 57–67. [CrossRef]
25. Jiang, Z.; Song, D.; Zeng, S. Prediction of Projectile—A Finite Cylindrical Cavity Expansion Theory and Its Application. *J. Vib. Shock* **2011**, *30*, 139–143+204. (In Chinese) [CrossRef]
26. Wang, J.; Zhao, J.; Zhang, J.; Zhou, Y. Study on Model of Penetration into Thick Metallic Targets with Finite Planar Sizes by Long Rods. *Shock Vib.* **2021**, *2021*, e6666770. [CrossRef]
27. Forrestal, M.J.; Okajima, K.; Luk, V.K. Penetration of 6061-T651 Aluminum Targets with Rigid Long Rods. *J. Appl. Mech.* **1988**, *55*, 755–760. [CrossRef]
28. Satapathy, S.; Bless, S. Calculation of Penetration Resistance of Brittle Materials Using Spherical Cavity Expansion Analysis. *Mech. Mater.* **1996**, *23*, 323–330. [CrossRef]
29. Tate, A. Long Rod Penetration Models—Part II. Extensions to the Hydrodynamic Theory of Penetration. *Int. J. Mech. Sci.* **1986**, *28*, 599–612. [CrossRef]
30. Recht, R.F. Taylor Ballistic Impact Modelling Applied to Deformation and Mass Loss Determinations. *Int. J. Eng. Sci.* **1978**, *16*, 809–827. [CrossRef]

Disclaimer/Publisher's Note: The statements, opinions and data contained in all publications are solely those of the individual author(s) and contributor(s) and not of MDPI and/or the editor(s). MDPI and/or the editor(s) disclaim responsibility for any injury to people or property resulting from any ideas, methods, instructions or products referred to in the content.